A Random Trajectory Approach for the Development of Non-Stationary Channel Models Capturing Different Scales of Fading

Alireza Borhani†, Gordon L. Stüber‡, and Matthias Pätzold†

† *Faculty of Engineering and Science, University of Agder*

P.O. Box 509, 4898 Grimstad, Norway

Emails: {alireza.borhani, matthias.paetzold}@uia.no

‡ *Faculty of Electrical and Computer Engineering, Georgia Institute of Technology*

Zip Code 30332, Atlanta, GA, United States

Email: stuber@ece.gatech.edu

Abstract

This paper introduces a new approach to develop stochastic non-stationary channel models, the randomness of which originates from a random trajectory of the mobile station (MS), rather than from the scattering area. The new approach is employed by utilizing a random trajectory model based on the primitives of Brownian fields (BFs), while the position of scatterers can be generated from an arbitrarily two-dimensional (2D) distribution function. The employed trajectory model generates random paths, along which the MS travels from a given starting point to a fixed predefined destination point. To capture the path loss, the gain of each multipath component is modelled by a negative power law applied to the travelling distance of the corresponding plane wave, while the randomness of the path travelled results in large-scale fading. It is shown that the local received power is well approximated by a Gaussian process in logarithmic scale even for a very limited number of scatterers. It is also shown that the envelope of the complex channel gain follows closely a Suzuki process, indicating that the proposed channel model superimposes small-scale fading and large-scale fading. The local power delay profile (PDP) and the local Doppler power spectral density (PSD) of the channel model are also derived and analyzed.

***Index Terms* — Non-stationary channels, random trajectory models, small-scale fading, large-scale fading, path loss, envelope of the complex channel gain, received power.**

I. INTRODUCTION

The demanding mobility features of communication technologies call for the need for advanced channel models (among other needs), in which non-stationary aspects of the channel are carefully taken into account. In this connection, many empirical and analytical investigations, e.g., [1]–[3] show that the stationary assumption for the channel is only valid for extremely short travelling distances [4]. Nevertheless, the number of non-stationary channel models [5]–[12] proposed in the literature is still very limited. A geometry-based non-stationary channel model for high-speed train communications has been developed very recently in [5]. A non-stationary channel model with fixed scattering volumes with an application in the rural land-mobile satellite environments has been developed in [6]. A non-stationary T-junction channel model with randomly distributed scatterers for vehicular communications was also proposed in [7]. The utilized path models in [5]–[7] do not support variations of the angle-of-motion (AOM) of the MS. This is in contrast with real-world moving scenarios in which the AOM varies along the travelling path. The non-stationary channel model proposed in [8] mitigates this contradiction by assuming that the AOM of the MS changes in time. The geometry-based non-stationary channel models proposed in [9] and [10] capture and analyze the effect moving scatterers, while this effect is automatically captured in the measurement-based non-stationary channel models developed in [4] and [11].

In the WINNER II class of channel models [13], incremental movements of the MS are connected by correlating large-scale channel parameters between these increments, resulting explicitly in a non-stationary channel model. The approach used to develop WINNER II channel models is a system-level approach, in which required channel characteristics, such as the angular spread, are first defined, and then the corresponding clusters of random scatterers are generated. A drawback of the channel models developed by this approach is the rigidity in capturing new channel characteristics once the model is developed [14]. In the COST family of channel models, e.g., COST 2100 [14], the movement of the MS in the propagation area causes the visibility of different clusters to change, resulting implicitly in a non-stationary channel model. The cluster-level approach employed to develop this family starts from generating a large quantity of clusters with randomly distributed scatterers inside, and then the synthetic channel characteristics are derived.

A similar approach to the development of non-stationary channel models is to update the

channel characteristics along the travelling path of the MS, which is surrounded by randomly distributed scatterers. For instance, the authors in [8], [15] provide a non-stationary one-ring channel model under the assumption that the MS is moving along a fixed trajectory surrounded by a ring of randomly distributed scatterers. In this paper, this approach is featured by allowing the trajectory of the MS to be random, while the position of the scatterers is fixed. This expansion adds considerably to the robustness of the channel model with respect to the number of scatterers, such that the desired statistical properties can be obtained even if the propagation area is sparsely seeded with scatterers. This is the major superiority of the channel models developed by this new approach to those developed by the existing approaches in the literature.

This paper utilizes a recently proposed [16], [17] random trajectory based on the primitives of BFs, along which the MS is assumed to move. The proposed trajectory model in [16] is able to generate many different configurations of the path with different smoothness levels. In this paper, the focus is on one important path configuration by which the arrival at a fixed predefined destination point is assured. To cope with the scattering effect of the propagation area, a 2D Gaussian probability density function (PDF) is employed to generate the positions of the scatterers. It is then assumed that the position of the scatterers is fixed, while the MS travels through the scattering area along a random path heading to a fixed destination point. Accordingly, the randomness of the channel model originates from the randomness of the trajectory, rather than that of the scattering area. We consider a fixed-to-mobile (F2M) frequency-selective communication scenario, in which the waves emitted from the base station (BS) antenna arrive at the MS antenna after a single bounce from every scatterer.

An additive complex channel gain model for the aforementioned propagation scenario is provided, in which not only the Doppler frequencies, but also the propagation path delays and the propagation path gains are stochastic processes that vary in position. In our model, the path gains are determined by a negative power law applied to the total travelling distance of the plane waves, which is in line with the basic idea of any path loss model. This paper also presents the angle-of-arrival (AOA) process and the AOM process, from which the Doppler frequency process is derived. The corresponding first-order densities are computed. Accordingly, the complex channel gain of the proposed non-stationary channel model is fully characterized. In addition, the first-order density of the channel gain envelope, the first-order density of the mean received power, as well as the local PDP and the local Doppler PSD are derived.

The simulation results confirm that the proposed channel model is non-stationary. Given a sparse scattering area, we show that the power of each incoming wave, the so-called received path power, follows closely the lognormal distribution. It is also proved that the sum of the received path powers, i.e., the total received power, is well approximated by a Gaussian process in logarithmic scale, indicating that the proposed channel model captures the effect of shadowing. The normality of the mean received power complies with the result reported in [18], where a ground-breaking additive model was considered as a physical basis for modelling shadow fading. Furthermore, it is shown that the envelope of the channel gain is well approximated by a Suzuki process, confirming that the proposed channel superimposes large-scale fading and small-scale fading. Noteworthy is that many measurement campaigns confirm that multi-scale fading channels under non-line-of-sight propagation conditions are best modelled by a Suzuki process [19], [20]. Moreover, it is shown that the proposed channel model has two degrees of freedom to control the spread of the shadowing. It is also demonstrated that the spread of the shadowing is approximately independent of the position of the BS. This also agrees with the empirical results reported, e.g., in [21]–[25]. In addition, our numerical results show that the mean received power decreases by increasing the BS-to-MS distance, affirming that the model captures the path loss effect as well. Finally, illustrative results reveal that the time-varying effect of each scatterer on the local PDP and the local Doppler PSD can perfectly be tracked if the channel is sufficiently sparse.

The novelty of the paper arises from the following features. The paper introduces a new approach to channel modelling under non-stationary conditions. This approach is also useful for the simulation/interpretation of measurement campaigns, in which a certain propagation area (fixed scattering area) undergoes several measurement trials (random trajectories). The proposed non-stationary channel model superimposes different levels of fading via a physically explainable multipath fading model, rather than a multiplicative one. The proposed channel model provides a physical (geometrical) insight to the theoretical studies in [18], [26]. The results provided in this paper are very useful for the development of mobile communication systems, e.g., for the design of Rake receivers [27], power control and handoff algorithms. It is also noteworthy that the contributions of [16] and this paper are fundamentally different. The main contribution of [16] is to develop a flexible trajectory model to capture mobility patterns with potential applications in different avenues of science, including social studies, emergency management, evacuation

modelling, and of course communications engineering. In this paper, we consider an application in mobile communications engineering, where the trajectory model is employed to develop a stochastic non-stationary channel model capturing different scales of fading.

The remainder of this paper is organized as follows. Section II introduces the concept of the new approach, while Sections III and IV employ the new approach to model the propagation area and the trajectory of the MS, respectively. The complex channel gain of the proposed non-stationary channel model is developed and characterized in Section V. The statistical properties of the channel model are analysed in Section VI, whereas the simulation results are provided in Section VII. Finally, Section VIII draws the conclusions.

II. The New Approach

The traditional approach in geometrical (statistical) channel modelling is to start from a geometric pattern filled by randomly distributed scatterers. A list of such models can be found in [28], [29]. The randomness of the position of scatterers is then injected to the characteristics of the channel model, such as its envelope, PDP, Doppler PSD, and correlation properties. One of the key factors influencing the characteristics of the channel models designed by this approach is obviously the number of scatterers. To provide a so-called reference model, this number is assumed to tend to infinity. In this paper, this is called the *infinity assumption*. The infinity assumption then allows designers to apply some limit theorems, such as the central limit theorem (CLT) of Lindeberg-Lévy, to conclude that the proposed channel model behaves like a Rayleigh, Rice, or lognormal (CLT for products) fading channel. The obvious shortcoming of these reference models is that the infinity assumption does not hold in real-world propagation scenarios. Even if the infinity assumption holds, moving through the propagation area would not be possible. Therefore, proposing any mobile radio channel model with an infinite number of scatterers is mathematically convenient but physically meaningless. Another issue is the restriction of computer-based simulation environments, where applying the infinity assumption is not possible. Accordingly, designers provide a so-called simulation model, in which the infinity assumption is relaxed by reducing the number of scatterers. However, this reduction degrades the characteristics of the channel model somewhat from those of reference models.

This paper introduces a new approach in which the randomness of the channel model originates from the randomness of the trajectory of the MS, while the scattering area remains fixed. The

positions of the scatterers are determined either by realizing any desired 2D distribution function, or by setting them manually. The new approach assumes a random trajectory, along which the MS is in motion through a fixed scattering area. Surveys of random trajectory models can be found in [30]–[32]. Very recently, a highly flexible random trajectory model based on the primitives of BFs has been proposed in [16]. Let us assume that the MS is moving along a random trajectory generated by a mobility model. For a fixed scattering area, each realization of the trajectory results in different AOMs of the MS, different AOAs at the MS, as well as different travelling distances of the plane wave emitted from the transmitter. Therefore, the randomness of the trajectory model is injected to the characteristics of the corresponding channel model. The motion of the MS along a given trajectory also allows us to capture the non-stationarity of the propagation area.

This paper shows that the main statistical properties of the non-stationary channel model developed by applying the new approach are very robust with respect to the number of scatterers. For instance, it is shown that the envelope of the complex channel gain closely follows a Suzuki process, even if the number of scatterers is only four. For the same number of scatterers, our findings demonstrate that the local received power follows the lognormal distribution, indicating that the channel model captures the shadow fading even for a very limited number of scatterers. The merit of the new approach is not only its robustness with respect to the number of scatterers, but also its capability to take the non-stationary aspects of the channel into account. Different scales of fading can also be captured if the channel model is developed properly. In what follows, we discuss how the new approach can be used to simulate a wide range of measurement campaigns.

Let us first remark that the random mobility models in the literature can be divided into two major categories [16]: 1) models that generate targeted trajectories, where each trajectory realization is unique, but subject to a predefined drift (destination point) and 2) models that generate non-targeted trajectories, where each trajectory realization results in a substantially different trajectory. Now recall the principles of the new approach based on tracking the MS and measuring the channel for different realizations of the trajectory surrounded by a fixed scattering area. If the random trajectories are targeted, different travelling scenarios in a fixed propagation area are somewhat simulated. A clear example is when the aim is to characterize an F2M channel along a street. If this experiment is repeated, minor changes of the travelling path are unavoidable,

whereas the scattering area is fixed for all trials. These minor changes are modelled by the targeted random trajectory. If the random trajectories are non-targeted, measurement campaigns carried out in distinct propagation areas are somewhat simulated. Notice that although, the new approach assumes that the scattering area is fixed, choosing totally different travelling routes (non-targeted trajectories) is almost similar to encountering different propagation areas.

It is noteworthy that with this approach, one may need a relatively large number of trials (random trajectories) to find the average channel characteristics, such as those reported empirically. Nonetheless, a large number of trials is in contrast neither with the potentials of any physical channel, nor with the capabilities of computer-based simulation tools, such as MATLAB®.

III. The Propagation Scenario

Fig. 1 demonstrates a typical F2M propagation scenario, where the MS is travelling through a scattering area, in which the BS is fixed and located at the distance D_0 from the origin of the Cartesian coordinate system. It is assumed that at a reference point in time t_0, the MS starts its motion from $(x(0), y(0))$ (or equivalently (x_s, y_s)) and moves along a random trajectory (see Section IV) to reach the terminating point $(x(L), y(L))$ at time t_L. Subsequently, the position of the MS along a random trajectory at time $t_l \in [t_0, t_L]$ is represented by Cartesian coordinates $(\boldsymbol{x}(l), \boldsymbol{y}(l))$, in which l denotes the corresponding position index. For a single realization of the trajectory (see Fig. 1), the position of the MS at t_l is shown by $(x(l), y(l))$. It is also assumed that a plane wave emitted from the BS arrives at the MS with the AOA $\boldsymbol{\alpha}_n^R(l)$ after only one bounce due to the nth scatterer S_n $(n = 1, 2, ..., N)$ located at (x_n^S, y_n^S). To reduce the mathematical complexity of the model, the elevation angular spread of the propagation waves[1] is ignored. This assumption allows us to adapt the 2D Brownian trajectory model discussed in Section IV to the proposed propagation model. It is also assumed that the MS is in motion with a constant speed[2] of v_R in the direction indicated by the AOM $\boldsymbol{\alpha}_v(l)$. It is also assumed that both the BS and the MS are equipped with a single omnidirectional antenna.

To obtain the position (x_n^S, y_n^S) of the scatterers, in principle, any 2D distribution function can be used. Herein, a 2D zero-mean Gaussian distribution with the standard deviation σ_s of 500 m

[1]Such a model is applicable in cellular systems when low height base station antennas are employed [33], [34].

[2]With reference to [35], a variation of the speed and/or the direction of the MS results in a non-stationary channel model.

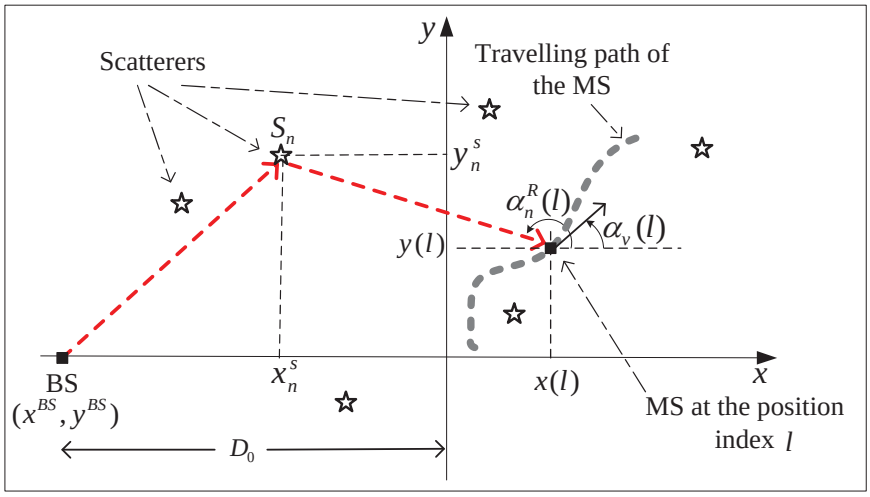

Fig. 1. A typical F2M propagation scenario assuming single-bounce scattering.

is used to generate a sparse scattering area with only $N = 4$ scatterers[3]. Fig. 2 demonstrates the results, where each scatterer has been marked by a different colour. The BS is placed at $(-500\,\mathrm{m}, 0\,\mathrm{m})$, meaning that the distance D_0 from the BS to the starting point of the MS is 500 m. Notice that owing to the sparsity of the channel, the position of the scatterers in Fig. 2 does not indicate a Gaussian distribution. Accordingly, these positions could be obtained by any other 2D distribution function. Therefore, it can be concluded that the results provided in this paper are not affected by changing the type of scatterer distribution function, provided that the channel is sufficiently sparse. The interpretation of the plotted random trajectories in Fig. 2 follows in the next section.

IV. The Trajectory Model

To run the new approach, a recently proposed trajectory model [16] based on the primitives of BFs is employed. According to this model, a path starting from (x_s, y_s) and terminating at or in the proximity of a predefined destination point (x_d, y_d) is modelled by the random trajectory

[3]Notice that the number of scatterers can be set to higher values, as it may be expected in real-world propagation environments. Nevertheless, to show the robustness of the proposed channel model with respect to the number of scatterers, as well as for enabling visual inspections, the channel is studied under sparse scattering conditions.

${}_p\mathcal{T}$ given by the following set of pairs

$$ {}_p\mathcal{T}: \left\{ ({}_p\boldsymbol{x}(l), {}_p\boldsymbol{y}(l)) \;\middle|\; \begin{array}{l} {}_p\boldsymbol{x}(l) = x_s + k_d\, l\delta_x + \sigma_x\, {}_p\boldsymbol{W}_x(l, k_b) \\ {}_p\boldsymbol{y}(l) = y_s + k_d\, l\delta_y + \sigma_y\, {}_p\boldsymbol{W}_y(l, k_b) \end{array} \right\} \tag{1} $$

for $l = 1, 2, ..., L$, where L is a positive integer. The terms $\delta_x = (x_d - x_s)/L$ and $\delta_y = (y_d - y_s)/L$ denote the deterministic increments along the x- and y-axis, respectively. The drift parameter k_d acts as a switch to control the presence of such a deterministic drift that forces the trajectory to evolve towards the destination point (x_d, y_d). The parameter σ_x (σ_y) controls the randomness of the trajectory process ${}_p\boldsymbol{x}(l)$ (${}_p\boldsymbol{y}(l)$) along the x-axis (y-axis).[4] Furthermore, the objective of the partial random bridge, defined as

$$ {}_p\boldsymbol{W}_x(l, k_b) = {}_p\boldsymbol{B}_x(l) - \frac{k_b\, l}{L}\, {}_p\boldsymbol{B}_x(L) \tag{2} $$

models the randomness of the trajectory along each axis by means of the pth primitive ${}_p\boldsymbol{B}_x(l)$ of the standard BF $\boldsymbol{B}_x(l)$ associated with the x-axis. The parameter k_b is called the bridge parameter, which determines the integration degree of the bridge to the destination point. In addition, the primitive p determines the smoothness level of the trajectory, which increases as p grows [16].

The trajectory ${}_p\mathcal{T}$ in (1) has been designed in such a way that it allows: 1) arriving at a predefined destination point (x_d, y_d) if the bridge is fully established, i.e., $k_b = 1$; 2) arriving at a target zone with a predefined radius and centre if the bridge is partially established, i.e., $0 < k_b < 1$; 3) a totally random point in the 2D plane if the bridge is broken, i.e., $k_b = 0$; and finally 4) bridging back (closed loop) to the starting point (x_s, y_s) if the bridge is fully established, i.e., $k_b = 1$, but the drift component does not exist, i.e., $k_d = 0$. The entire set of configurations above plus several others have been shown and discussed in [16]. From the configurations above, it can be concluded that ${}_p\mathcal{T}$ in (1) allows for the generation of both targeted and non-targeted random trajectories (see Section II). One of the novel features of ${}_p\mathcal{T}$ in (1) is its representation in position, rather than time. This allows us to test different speed scenarios without influencing the trajectory configuration (see [16]).

In this paper, a special case of the random trajectory in (1) is considered, where the first primitive of BFs is employed, i.e., $p = 1$, and the random bridge to the destination point (x_d, y_d)

[4]Note that owing to the symmetry of the trajectory model, the statistical properties of ${}_px(l)$ and ${}_py(l)$ are the same.

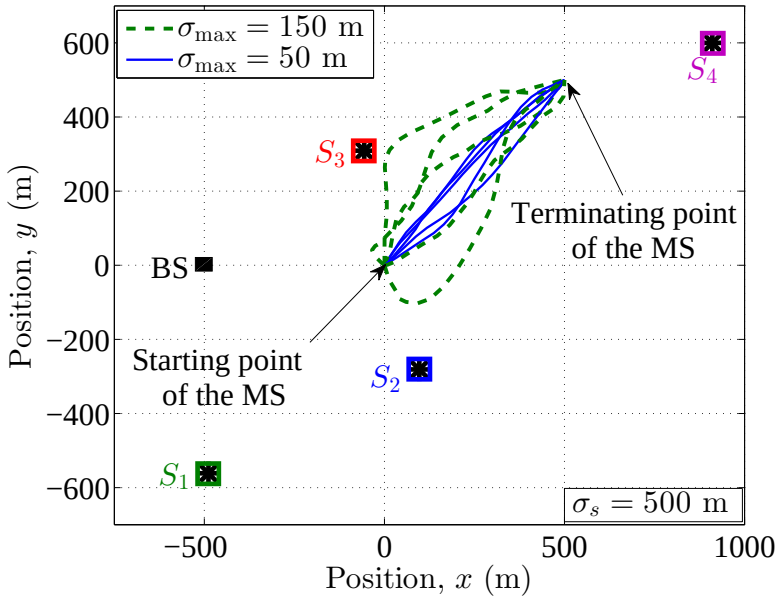

Fig. 2. A simulated sparse scattering area ($N = 4$), illustrating several realizations of the random trajectory $\mathcal{T}$ in (1), where $L = 20$.

is fully established, i.e., $k_b = k_d = 1$. This means that the model parameters are chosen such that the trajectory model generates targeted random travelling paths. For such a special case, it has been shown in [16] that if $\sigma_x = \sigma_y$, the random trajectory takes its maximum distance from the shortest trajectory (straight line from the starting point to the destination point) at the position index $l = L/2$. This maximum distance is denoted by $\sigma_{\max}$, which equals $\sigma_x \sqrt{L^3/48}$. Since investigating the effect of the primitive p is outside of the scope of this paper, we henceforth drop the index p from the notations.

Fig. 2 displays several realizations of the random trajectory $\mathcal{T}$ in (1) for two different values of $\sigma_{\max}$. It is assumed that the origin $(0\,\mathrm{m}, 0\,\mathrm{m})$ of the Cartesian coordinates is the starting point of the travelling path, whereas the point located at $(500\,\mathrm{m}, 500\,\mathrm{m})$ is the destination point.

A different random trajectory model may be used to develop a stochastic non-stationary channel model by means of the proposed approach in Section II. The flexibility and the usefulness of the random trajectory model in [16] motivates us to choose it for generating the path of the MS. In this context, it has been shown in both [16], [17] that the random trajectory in (1)

captures many realistic mobility patterns, while the spatial properties of the path follow those of real-world user tracings.

V. The Complex Channel Gain Process

To model the complex channel gain of the propagation scenario (see Figs. 1 and 2), the model in [36, pp. 45–48] is extended by considering the principles of non-stationary multiple-component signals discussed in [37, pp. 19–21]. This expansion allows the Doppler frequencies[5] $\boldsymbol{f}_n(l)$, propagation path delays $\boldsymbol{D}_n(l)$, and the propagation path gains $\boldsymbol{c}_n(l)$ to vary in the position index l. Accordingly, this paper models the complex channel gain $\boldsymbol{\mu}(t_l)$ by means of the following expression

$$\begin{aligned} \boldsymbol{\mu}(t_l) &= \sum_{n=1}^{N} \boldsymbol{\mu}_n(t_l) \\ &= \sum_{n=1}^{N} \boldsymbol{c}_n(t_l) e^{j\left(2\pi \int_{-\infty}^{t_l} \boldsymbol{f}_n(t_l')dt_l' - k_0 \boldsymbol{D}_n(t_l) + \boldsymbol{\phi}_n\right)} \end{aligned} \tag{3}$$

representing the sum of all scattered components $\boldsymbol{\mu}_n(t_l)$ in time[6]. In this equation, $k_0 = 2\pi/\lambda_0$ denotes the free-space wave number, where λ_0 is the wavelength. The random variable $\boldsymbol{\phi}_n$ represents the phase shift of the nth propagation path caused by the physical interaction of the transmitted signal with the nth scatterer S_n. It is often assumed that the phases $\boldsymbol{\phi}_n$ are independently and identically distributed random variables, each of which is uniformly distributed between $-\pi$ and π (see, e.g., [36, p. 47] and [39, p. 59]).

The corresponding time-variant impulse response of the multipath frequency-selective channel can then be expressed by $\boldsymbol{h}(\tau', t_l) = \sum_{n=1}^{N} \boldsymbol{\mu}_n(t_l)\delta(\tau' - \boldsymbol{\tau'}_n(t_l))$, in which $\delta(\cdot)$ represents the Dirac delta function and the propagation delay $\boldsymbol{\tau'}_n(t_l)$ associated with the nth scatterer equals $c_0^{-1}\boldsymbol{D}_n(l)$.

Recall the trajectory model provided in Section IV. It is assumed that the position of the MS is given by the pair of stochastic processes $(\boldsymbol{x}(l), \boldsymbol{y}(l))$ in (1). Furthermore, suppose that one

[5]The frequency shift caused by the Doppler effect is given by $\boldsymbol{f} = f_{\max}\cos(\boldsymbol{\alpha})$, where $f_{\max} = f_0 v/c_0$ is the maximum Doppler frequency, f_0 denotes the carrier frequency, c_0 stands for the speed of light, and $\boldsymbol{\alpha}$ equals the difference between the AOA and the AOM [38].

[6]For the sake of brevity of notations, henceforth, the time t_l is replaced/briefed by the position index l, unless the temporal representation helps to the clarity of the subject.

realization of the Gaussian scattering area is given (see Fig. 2), which allows us to determine the position (x_n^S, y_n^S) of all N scatterers. Thus, one can represent the model parameters $\boldsymbol{f}_n(l)$, $\boldsymbol{D}_n(l)$, and $\boldsymbol{c}_n(l)$ as stochastic processes that vary in the position index l. As a special case, these parameters become deterministic values if only one realization of the trajectory $\mathcal{T}$ is considered. Nevertheless, one still may have a stochastic complex channel gain $\boldsymbol{\mu}(t_l)$ if the phase shifts $\boldsymbol{\phi}_n$ are random. Another option to obtain a stochastic complex channel gain $\boldsymbol{\mu}(t_l)$ is to focus on a single trajectory realization, while the scattering area is assumed to be random [8]. In what follows, the parameters of the complex channel gain $\boldsymbol{\mu}(t_l)$ in (3) are studied in detail.

A. Propagation Path Length Process $\boldsymbol{D}_n(l)$

Referring to Fig. 1, the total travelling distance $\boldsymbol{D}_n(l)$ of the nth plane wave is the sum of a constant distance D_n^{BS-S} from the BS to the position (x_n^S, y_n^S) of the nth scatterer S_n and a random distance $\boldsymbol{D}_n^{S-MS}(l)$ from S_n to the position $(\boldsymbol{x}(l), \boldsymbol{y}(l))$ of the MS, i.e.,

$$\begin{aligned}\boldsymbol{D}_n(l) &= D_n^{BS-S} + \boldsymbol{D}_n^{S-MS}(l) \\ &= \sqrt{(y^{BS}-y_n^S)^2+(x^{BS}-x_n^S)^2} + \sqrt{(y_n^S-\boldsymbol{y}(l))^2+(x_n^S-\boldsymbol{x}(l))^2}. \end{aligned} \tag{4}$$

Theorem 1. Let $m_{\boldsymbol{x}}(l)$ ($m_{\boldsymbol{y}}(l)$) and $\sigma_{\boldsymbol{x}}(l)$ ($\sigma_{\boldsymbol{y}}(l)$) denote the mean and the standard deviation of the process $\boldsymbol{x}(l)$ ($\boldsymbol{y}(l)$) in (1), respectively. The first-order density $p_{\boldsymbol{D}_n}(d_n; l)$ of the total travelling distance process $\boldsymbol{D}_n(l)$ in (4) is given by

$$\begin{aligned} p_{\boldsymbol{D}_n}(d_n;l) &= \frac{d_n - D_n^{BS-S}}{\sigma_{\boldsymbol{x}}^2(l)} \exp\left\{-\frac{(x_n^S - m_{\boldsymbol{x}}(l))^2 + (y_n^S - m_{\boldsymbol{y}}(l))^2 + (d_n - D_n^{BS-S})^2}{2\sigma_{\boldsymbol{x}}^2(l)}\right\} \\ &\times I_0\left(\frac{\sqrt{(x_n^S - m_{\boldsymbol{x}}(l))^2 + (y_n^S - m_{\boldsymbol{y}}(l))^2}}{\sigma_{\boldsymbol{x}}^2(l)}(d_n - D_n^{BS-S})\right) \end{aligned} \tag{5}$$

where $\sigma_{\boldsymbol{x}}(l) = \sigma_{\boldsymbol{y}}(l)$ and $I_0(\cdot)$ denotes the zeroth order modified Bessel function of the first kind.

Proof: See Appendix A. ■

From Theorem 1, the first-order density $p_{\boldsymbol{\tau'}_n}(\tau_n'; l)$ of the propagation delay process $\boldsymbol{\tau'}_n(l)$ can be derived. It is straightforward to show that $p_{\boldsymbol{\tau'}_n}(\tau_n'; l)$ is given by $p_{\boldsymbol{\tau'}_n}(\tau_n'; l) = c_0\, p_{\boldsymbol{D}_n}(c_0\tau_n'; l)$.

B. Propagation Path Gain Process $\boldsymbol{c}_n(l)$

With the objective to model Rayleigh and Rice processes, one of the widely made assumptions in the literature (see, e.g., [39, p. 85]) is that the path gains $\boldsymbol{c}_n(l)$ are equal, deterministic, and

independent of the propagation path length $\boldsymbol{D}_n(l)$. We relax these assumptions by allowing the path gains to be determined by $\boldsymbol{c}_n(l) = C\boldsymbol{D}_n^{-\gamma/2}(l)$, where $\boldsymbol{D}_n(l)$ is the total travelling distance of the nth path given in (4). The idea of this formulation originates from the fundamental concept of any path loss model, according to which the received power (herein, the received path power $c_n^2(l)$) reduces by a negative power law (controlled by γ) if the travelling distance (herein, $D_n(l)$) of the corresponding plane wave increases. This formulation also captures the definition of the path magnitude provided in [36, p. 47]. The power law γ is often called the path loss exponent, which has been reported to be $\gamma = 2$ in the free space, while it ranges from 3 to 5 in rural and urban areas. Moreover, the constant C accounts for the total transmission power, antenna(s) gain, wave length, number of scatterers N, and a few more physical parameters (see [40], [41]).

The propagation path gain process $\boldsymbol{c}_n(l)$ is a non-linear transformation of the path length process $\boldsymbol{D}_n(l)$. Therefore, its first-order density $p_{\boldsymbol{c}_n}(y_n; l)$ can be obtained by applying the concept of transformation of random variables [42, p. 130]. It follows

$$p_{\boldsymbol{c}_n}(y_n; l) = \frac{2}{\gamma}\left(C^2 y_n^{-(\gamma+2)}\right)^{\frac{1}{\gamma}} \times p_{\boldsymbol{D}_n}((C^2 y_n^{-2})^{\frac{1}{\gamma}}; l) \tag{6}$$

where $p_{\boldsymbol{D}_n}(\cdot; l)$ is the first-order density of $\boldsymbol{D}_n(l)$ given in Theorem 1. Note that path loss coefficients $c_n(l)$ vary in both n (with the position of scatterers) and l (with the position of the MS). These coefficients follow the first-order density in (6), the randomness of which originates from the randomness of the trajectory in (1).

Of great interest is also the first-order density $p_{\boldsymbol{c}_n^2}(y_n; l)$ of $\boldsymbol{c}_n^2(l)$, namely the received path power associated with the nth plane wave. It can be shown that $p_{\boldsymbol{c}_n^2}(y_n; l)$ can be presented in the following form

$$p_{\boldsymbol{c}_n^2}(y_n; l) = \frac{1}{\gamma}\left(C^2 y_n^{-(\gamma+1)}\right)^{\frac{1}{\gamma}} \times p_{\boldsymbol{D}_n}((C^2 y_n^{-1})^{\frac{1}{\gamma}}; l). \tag{7}$$

It can be shown (not provided here) that $p_{\boldsymbol{c}_n^2}(y_n; l)$ follows closely the first-order density of a lognormal process, which tends to a delta function as l tends to 0 and/or L. This is due to that fact that the starting and terminating points of $\mathcal{T}$ in (1) are fixed (realization-independent). Notice that this does not limit the applicability of the proposed non-stationary channel model, as by changing the parameters of the trajectory model in (1), one can generate random trajectories that do not necessarily terminate at a fixed destination point. In this case, the received path power $\boldsymbol{c}_n^2(L)$ becomes a random variable, rather than a fixed value.

C. Doppler Frequency Process $\boldsymbol{f}_n(l)$

The local Doppler frequency $\boldsymbol{f}_n(l)$ is defined by a non-linear transformation of the local AOA $\boldsymbol{\alpha}_n^R(l)$ and the local AOM $\boldsymbol{\alpha}_v(l)$ of the MS. It follows

$$\boldsymbol{f}_n(l) = f_{\max} \cos\left(\boldsymbol{\alpha}_n^R(l) - \boldsymbol{\alpha}_v(l)\right) \tag{8}$$

where $\boldsymbol{\alpha}_n^R(l)$ and $\boldsymbol{\alpha}_v(l)$ are given by (see Fig. 1)

$$\boldsymbol{\alpha}_n^R(l) = \arctan\left(\frac{y_n^S - \boldsymbol{y}(l)}{x_n^S - \boldsymbol{x}(l)}\right) \tag{9}$$

and

$$\boldsymbol{\alpha}_v(l) = \arctan\left(\frac{\boldsymbol{y}(l+1) - \boldsymbol{y}(l)}{\boldsymbol{x}(l+1) - \boldsymbol{x}(l)}\right) \tag{10}$$

for $l = 0, 1, ..., L-1$, respectively.

Theorem 2. The first-order density $p_{\boldsymbol{\alpha}_n^R}(\alpha_n; l)$ of the AOA process $\boldsymbol{\alpha}_n^R(l)$ in (9) is given by

$$\begin{aligned} p_{\boldsymbol{\alpha}_n^R}(\alpha_n; l) \;=\; & \frac{1}{2\pi} \exp\left\{-\left(\frac{(x_n^S - m_{\boldsymbol{x}}(l))^2 + (y_n^S - m_{\boldsymbol{y}}(l))^2}{2\sigma_{\boldsymbol{x}}^2(l)}\right)\right\} \\ & \times \left(1 + \sqrt{2\pi} g(\alpha_n; l) \operatorname{erfc}\left(-\sqrt{2} g(\alpha_n; l)\right) \exp\left\{2g^2(\alpha_n; l)\right\}\right) \end{aligned} \tag{11}$$

where

$$g(\alpha_n; l) = \frac{1}{2\sigma_{\boldsymbol{x}}(l)} \left((x_n^S - m_{\boldsymbol{x}}(l)) \cos(\alpha_n) + (y_n^S - m_{\boldsymbol{y}}(l)) \sin(\alpha_n)\right) \tag{12}$$

and $\operatorname{erfc}(\cdot)$ stands for the complementary error function [43, p. 887].

Proof: Following the discussion in the proof of Theorem 1, the AOA process $\boldsymbol{\alpha}_n^R(l)$ in (9) can be considered as the phase of a complex Gaussian process with $(x_n^S - \boldsymbol{x}(l))$ and $(y_n^S - \boldsymbol{y}(l))$ as the inphase and quadrature component, respectively. The phase of complex Gaussian processes with correlated components and non-identical means (variances) has been studied in [44] and [45]. Setting $\rho = 0$ in [45, Eq. (2)] and performing some mathematical manipulations results in (11). ■

The first-order density $p_{\boldsymbol{\alpha}_v}(\alpha_n; l)$ of the AOM process $\boldsymbol{\alpha}_v(l)$ in (10) has been derived in [17]. Accordingly, the elements $\boldsymbol{\alpha}_n^R(l)$ and $\boldsymbol{\alpha}_v(l)$ of the local Doppler frequency process $\boldsymbol{f}_n(l)$ in (8) are completely determined. Nonetheless, deriving an analytical expression for the first-order density $p_{\boldsymbol{f}_n}(f_n; l)$ of the Doppler frequency $\boldsymbol{f}_n(l)$ is cumbersome, particularly because $\boldsymbol{\alpha}_n^R(l)$ and $\boldsymbol{\alpha}_v(l)$ are not statistically independent processes. Therefore, the behaviour of $\boldsymbol{f}_n(l)$ is studied by means of simulations (see Section VII).

VI. Channel Characteristics

In this section, other important characteristics of the channel, such as the envelope (of the complex channel gain) process, local received power process, local PDP process, as well as the local Doppler PSD (of the Doppler frequencies) process are investigated.

A. Envelope Process

Let $\boldsymbol{\zeta}(t_l)$ denote the envelope of the complex channel gain $\boldsymbol{\mu}(t_l)$ in (3), i.e., $\boldsymbol{\zeta}(t_l) = |\boldsymbol{\mu}(t_l)|$. By fixing the position index l and using the result in [46, Eq. (18)], it follows that the first-order density $p_{\boldsymbol{\zeta}}(z;l)$ of the envelope process $\boldsymbol{\zeta}(t_l)$ is given by

$$p_{\boldsymbol{\zeta}}(z;l) = (2\pi)^2 z \int_0^\infty \left[\prod_{n=1}^{N} \int_0^\infty p_{\boldsymbol{c}_n}(y_n;l) J_0(2\pi\, y_n x)\, dy_n \right] J_0(2\pi\, zx) x\, dx \tag{13}$$

where $p_{\boldsymbol{c}_n}(y_n;l)$ is the first-order density of the propagation path gain $\boldsymbol{c}_n(l)$ provided in (6), and $J_0(\cdot)$ stands for the zeroth-order Bessel function of the first kind [43, Eq. (8.411.1)]. In agreement with [39, p. 131], the Doppler frequency $\boldsymbol{f}_n(l)$ and the phase shift $\boldsymbol{\phi}_n$ have no influence on $p_{\boldsymbol{\zeta}}(z;l)$. However, $p_{\boldsymbol{\zeta}}(z;l)$ is a function of the path gains $\boldsymbol{c}_n(l)$, which are here allowed to change with the propagation path length $\boldsymbol{D}_n(l)$ (see Section V-B). Moreover, referring to (13), $p_{\boldsymbol{\zeta}}(z;l)$ varies in the position index l, indicating that the envelope process $\boldsymbol{\zeta}(t_l)$ is non-stationary in the strict sense. In Section VII, it is shown that depending on l, $p_{\boldsymbol{\zeta}}(z;l)$ can be approximated by the first-order density of different standard processes, including the Rayleigh, lognormal, Weibull, and the Suzuki process. However, the goodness-of-fit is not always acceptable. Among the aforementioned candidates, it is shown that the Suzuki process always gives the best fit to $p_{\boldsymbol{\zeta}}(z;l)$ in (13). This agrees completely with many empirical studies, reporting that physical channels with both small-scale and large-scale fading are best modelled by the Suzuki process [19], [20]. Notice that the Suzuki process is a product process of a Rayleigh process and a lognormal process. Notice that the aim of this paper is not to decompose the envelope $\boldsymbol{\zeta}(t_l)$ into Rayleigh and lognormal processes, but to show that $\boldsymbol{\zeta}(t_l)$ superimposes small-scale fading and large-scale fading (see [20]).

B. Local Received Power

For a given trajectory, the local received power $\boldsymbol{\Omega}(l)$ averaged over the random phase is obtained by the conservation-of-power law [50], according to which

$$\boldsymbol{\Omega}(l) = \sum_{n=1}^{N} \boldsymbol{c}_n^2(l) \tag{14}$$

where $\boldsymbol{c}_n^2(l) = C^2 \boldsymbol{D}_n^{-\gamma}(l)$ in Watts is the position-dependent received path power associated with the nth incoming plane wave (Proof: See Appendix B).

The first-order density $p_{\boldsymbol{\Omega}}(\omega; l)$ of the total received power $\boldsymbol{\Omega}(l)$ can then be obtained by the following expression

$$p_{\boldsymbol{\Omega}}(\omega; l) = \int_{-\infty}^{+\infty} \Psi_{\boldsymbol{\Omega}}(\nu; l) e^{j2\pi\nu\omega}\, d\nu \tag{15}$$

in which $\Psi_{\boldsymbol{\Omega}}(\nu; l)$ represents the characteristic function of the total received power $\boldsymbol{\Omega}(l)$. This function is the result of the product

$$\Psi_{\boldsymbol{\Omega}}(\nu; l) = \prod_{n=1}^{N} \Psi_{\boldsymbol{c}_n^2}(\nu; l) \tag{16}$$

where $\Psi_{\boldsymbol{c}_n^2}(\nu; l)$ denotes the characteristic function of the received path power $\boldsymbol{c}_n^2(l)$. The function $\Psi_{\boldsymbol{c}_n^2}(\nu; l)$ is attained by taking the complex conjugate of the Fourier transform of the first-order density $p_{\boldsymbol{c}_n^2}(y_n; l)$ of $\boldsymbol{c}_n^2(l)$ in (7), i.e.,

$$\Psi_{\boldsymbol{c}_n^2}(\nu; l) = \int_{-\infty}^{+\infty} p_{\boldsymbol{c}_n^2}(y_n; l) e^{j2\pi\nu y_n}\, dy_n. \tag{17}$$

Providing a closed-form expression for the integral above is not possible. Nevertheless, this does not affect our understanding of the distribution of the total received power $\boldsymbol{\Omega}(l)$. Recall that the received path power $\boldsymbol{c}_n^2(l)$ can be well approximated by a lognormal process (see Sections V-B and VII). It has been shown theoretically that not only a sum of a few lognormal processes, but also that of a large number of lognormal processes can be approximated by a lognormal process [18], [26], [47]. Therefore, it can be concluded that the total received power $\boldsymbol{\Omega}(l)$ in (14) follows approximately a lognormal process both in sparse and rich scattering areas. In Section VII, the numerical results show that for the considered sparse scattering area ($N = 4$), the local received power $\boldsymbol{\Omega}(l)$ follows closely the normal distribution in logarithmic scale.

It is remarkable that the additive model proposed in [18] provides a physical basis for shadow fading, whereas the traditional multiplicative approach is hard to be explained physically. In [18], different distributions of $\boldsymbol{c}_n^2(l)$, including the lognormal, gamma, chi-square, and the Weibull distribution, have been employed to show that the sum in (14) follows the Gaussian distribution in logarithmic scale. However, the reason for these choices was never discussed. This paper provides a geometrical insight to the additive shadow fading model presented in [18], in which the distribution of $\boldsymbol{c}_n^2(l)$ is determined by a physical measure, namely the travelling distance $\boldsymbol{D}_n(l)$ of the nth plane wave (see Section V-B). Nonetheless, the objective of our paper is not to give a physical explanation for the shadow fading.

C. Local Power Delay Profile

The PDP of stationary channel models is obtained by the product of the time-invariant received power and the PDF of the propagation delays. In reality, however, both the received power and the propagation delay process vary in time (position). The non-stationary channel model proposed in this paper takes these variations into account. Accordingly, the definition of the PDP is expanded to the following local PDP

$$S_{\boldsymbol{\tau'}}(\tau';l) = \sum_{n=1}^{N} m_{\boldsymbol{c}_n^2}(l) p_{\boldsymbol{\tau'}_n}(\tau'_n;l) \tag{18}$$

where

$$m_{\boldsymbol{c}_n^2}(l) = \int_{-\infty}^{\infty} y_n \, p_{\boldsymbol{c}_n^2}(y_n;l)\, dy_n \tag{19}$$

is the mean received power of the nth path and $p_{\boldsymbol{\tau'}_n}(\tau'_n;l)$ is the first-order density of the delay $\tau'_n(l)$ (see Section V-A). Furthermore, $p_{\boldsymbol{c}_n^2}(y_n;l)$ is the first-order density of the received path power associated with the nth incoming plane wave (see (7)).

D. Local Doppler Power Spectral Density

The Doppler PSD of stationary channel models is the product of the time-invariant received power and the PDF of the Doppler frequencies. These quantities are, however, time-variant in practice. The local Doppler PSD is then given by

$$S_{\boldsymbol{\mu\mu}}(f;l) = \sum_{n=1}^{N} m_{\boldsymbol{c}_n^2}(l) p_{\boldsymbol{f}_n}(f;l) \tag{20}$$

in which $p_{\boldsymbol{f}_n}(f_n; l)$ denotes the first-order density of the Doppler frequency $\boldsymbol{f}_n(l)$. As discussed in Section V-C, presenting $p_{\boldsymbol{f}_n}(f_n; l)$ in a closed form is cumbersome. Nonetheless, numerical techniques (see Section VII) assist us to illustrate and analyze the local Doppler PSD $S_{\boldsymbol{\mu\mu}}(f; l)$ in (20).

VII. Simulation Results

A. Parameter Settings and Procedures

Given is the propagation area shown in Fig. 2, in which the $N = 4$ scatterers are distinguished in four different colours. We again emphasize that the number of scatterers can be set to a higher value. Nonetheless, to demonstrate the robustness of the proposed channel model with respect to the number of scatterers, as well as for enabling visual inspections, the simulations are performed under sparse scattering conditions. Recall from Fig. 2 that the MS starts its motion from the origin $(0\,\mathrm{m}, 0\,\mathrm{m})$ of the Cartesian coordinates and travels toward the destination point located at $(500\,\mathrm{m}, 500\,\mathrm{m})$. In addition, it is assumed that the BS is located at $(-500\,\mathrm{m}, 0\,\mathrm{m})$. The operating frequency $f_0 = 2.1\,\mathrm{GHz}$ of the universal mobile telecommunications system (UMTS) is considered in our numerical computations. The speed of the MS is supposed to be $30\,\mathrm{km/h}$, which allows for a maximum Doppler frequency $f_{\max}$ of about 60 Hz. Furthermore, we consider the free space path loss exponent, i.e., $\gamma = 2$, as we believe that it suits more to our lossless single-bounce scattering scenario. Nevertheless, the effect of increasing γ will also be illustrated and discussed. The constant C is assumed to be 0.05 $\mathrm{W}^{1/2}\,\mathrm{m}$ (see Section V-B). As stated before, the parameters of the path model have been set such that arriving at the destination point $(500\,\mathrm{m}, 500\,\mathrm{m})$ via a relatively smooth trajectory is assured (see Section IV). The trajectory consists of 21 points indexed by $l = 0$ (starting point) until $l = L = 20$ (terminating/destination point). We also assume that the time t_l associated with each position index l does not vary in the realization.

The simulation results have been produced by taking the following steps: 1) The positions of $N = 4$ scatterers are generated by means of a 2D Gaussian distribution with zero mean and variance $\sigma_s = 500\,\mathrm{m}$. 2) The trajectory $\mathcal{T}$ in (1) has been realized for about 5000 times. 3) Each time, the total travelling distance $\boldsymbol{D}_n(l)$ (see 4), the local AOA $\boldsymbol{\alpha}_n^R(l)$ (see 9), and the local AOM $\boldsymbol{\alpha}_v(l)$ (see 10) have been measured. From the measured quantities, 4) the characteristics of interest, including the channel envelope, local received power, local PDP, and the local Doppler

PSD have been computed. As an example, for a given position index l, we have transformed the measured $\boldsymbol{D}_n(l)$ via $\boldsymbol{c}_n(l) = C\boldsymbol{D}_n^{-\gamma/2}(l)$ to obtain the received path power associated with the nth scatterer. The entire $N = 4$ path powers have then been summed up to attain the total received power $\Omega(l)$. This has been done for 5000 realizations of the trajectory. 5) The corresponding normalized histograms containing a proper number of equally spaced bins have been generated and the results have been shown in the form of a PDF.

In what follows, the simulation results are demonstrated and discussed extensively. For fluency reasons, the results are not necessarily presented in the same order as they are derived.

B. Results

Fig. 3 illustrates the PDF $p_{\boldsymbol{\zeta}}(z; l)$ of the envelope $\boldsymbol{\zeta}(t_l)$ in (13) for two different values of l. The best standard curves to each $p_{\boldsymbol{\zeta}}(z; l)$ have also been fitted. At $l = 4$ (almost the first quarter of the travelling path), the envelope $\boldsymbol{\zeta}(t_4)$ can be well approximated by all of the standard candidates, excluding the lognormal distribution. For $l = 10$ (almost in the middle of the travelling path), $\boldsymbol{\zeta}(t_{10})$ follows closely the Suzuki distribution, but neither the lognormal nor the Rayleigh distribution. Notice that $p_{\boldsymbol{\zeta}}(z; 10)$ is almost bounded by the PDFs of the lognormal and the Rayleigh distribution, indicating that the proposed channel behaves as a lognormal-Rayleigh fading channel, which is often called a Suzuki fading channel. The loglikelihood [48] goodness-of-fit metric has been used to conclude that the Suzuki process always gives the best fit to the envelope of the proposed multi-scale fading non-stationary channel model. Since assessing the goodness-of-fit by visual inspections is straightforward for most of the position indices ls, the results of the loglikelihood test are omitted herein. Notice that by increasing l, the mean of the envelope $\boldsymbol{\zeta}(t_l)$ decreases. This can be attributed to the fact that, by increasing the distance between the BS and the MS, the attenuation effect of the scattering area on the plane waves increases.

Fig. 4 demonstrates the PDF $p_{\boldsymbol{\Omega}}(\omega; 10)$ (see (15)) of the total received power $\boldsymbol{\Omega}(10)$ in logarithmic scale, where the position index l has been set to 10 (almost in the middle of the travelling path). Notice that according to (15), $p_{\boldsymbol{\Omega}}(\omega; l)$ varies in l (see Fig. 7). To boost the visibility of the figure, only $p_{\boldsymbol{\Omega}}(\omega; 10)$, but for different values of $\sigma_{\max}$, is displayed. The excellent match between the simulation results and the analytical ones confirms the correctness of (15). The best Gaussian fit to each plot has also been displayed. As can be observed, for

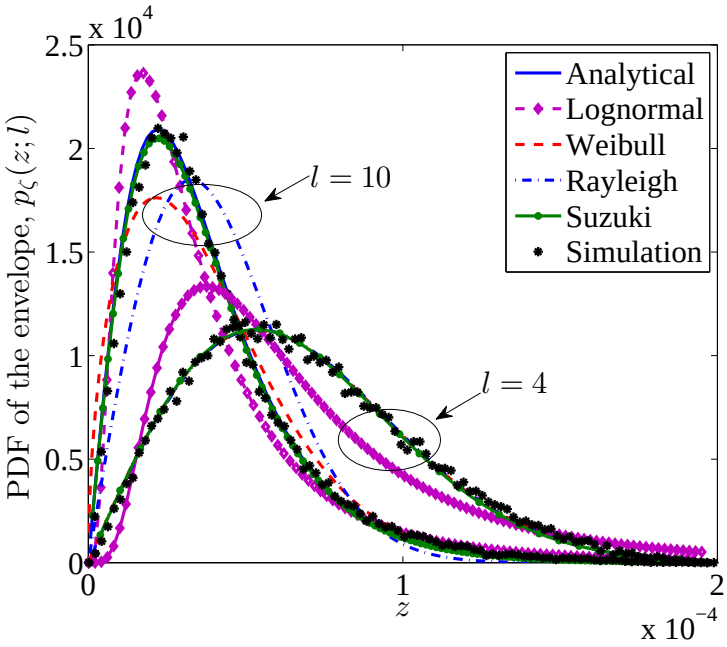

Fig. 3. The PDF $p_{\boldsymbol{\zeta}}(z;l)$ (see (13)) of the envelope $\boldsymbol{\zeta}(t_l)$ associated with the position index l.

different values of $\sigma_{\max}$, the total received power $\boldsymbol{\Omega}(10)$ follows closely the normal distribution, which allows us to conclude that the proposed channel model captures the so-called shadow fading. It is also important to mention that by increasing $\sigma_{\max}$, the spread of the received power increases. This is supported by Fig. 2, where increasing $\sigma_{\max}$ results in increasing the variations of the total travelling distance $\boldsymbol{D}_n(l)$ of each trajectory. Notice that $\boldsymbol{D}_n(l)$ is directly proportional to the local received power $\boldsymbol{\Omega}(l)$ (see Section V-B) and that the standard deviation $\sigma_\Omega(10)$ of the local received power can be controlled by the variance of the random trajectory.

Fig. 5 shows the effect of the path loss exponent γ on the standard deviation $\sigma_\Omega(10)$ of the local received power at the position index $l = 10$. The value of $\sigma_\Omega(l)$ is obtained by computing the square root of the second central moment of $\Omega(l)$. Referring to this figure, for a given $\sigma_{\max}$, the value of $\sigma_\Omega(10)$ increases by growing γ. This can also be supported by the path gain model proposed in Section V-B, where increasing γ magnifies the variations of the total travelling distance $\boldsymbol{D}_n(10)$. This figure allows us to conclude that the standard deviation $\sigma_\Omega(10)$ of the local received power can be controlled not only by $\sigma_{\max}$, but also by γ. Therefore, the proposed channel model provides two degrees of freedom for controlling the spread of the shadow fading.

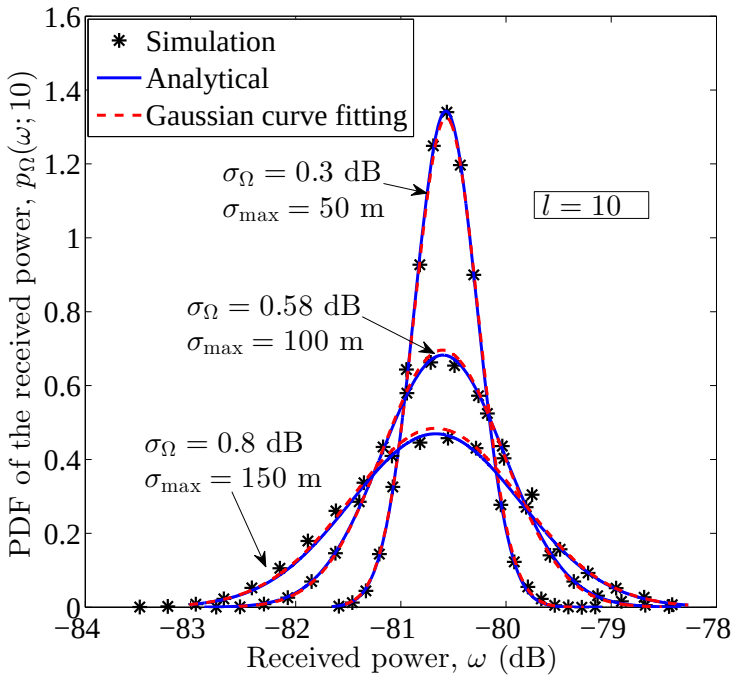

Fig. 4. The PDF $p_{\mathbf{\Omega}}(\omega; 10)$ (see (15)) of the local received power $\mathbf{\Omega}(10)$ in logarithmic scale for different values of $\sigma_{\max}$.

In addition, according to Fig. 5, the proposed channel model is able to generate large-scale fading with a spread between 0.25 dB and 2.75 dB. This range covers the empirically reported range from 0.85 dB to 2 dB measured in outdoor environments [49]. Furthermore, changing the two degrees of freedom allows us to obtain even higher spreads such as those reported in [27].

The standard deviation $\sigma_\Omega(10)$ of the local received power versus the distance D_0 of the BS from the origin is depicted in Fig. 6. As can be observed, by increasing D_0, the value of $\sigma_\Omega(10)$ remains approximately constant. This is consistent with the results of many measurement campaigns, such as those reported in [18], [21]–[25]. It is worth mentioning that by increasing the value of $\sigma_{\max}$, $\sigma_\Omega(10)$ cannot be well approximated by a constant value.

Fig. 7 displays the mean $m_\Omega(l)$ and the spread $\sigma_\Omega(l)$ of the local received power by the decreasing dashed-line and the solid vertical bars (the length of the bars), respectively. The minimum and the maximum of the local received power (see Fig. 4) obtained by simulation results have also been merged into this figure. Notable is the fact that $m_\Omega(l)$ shows the time-

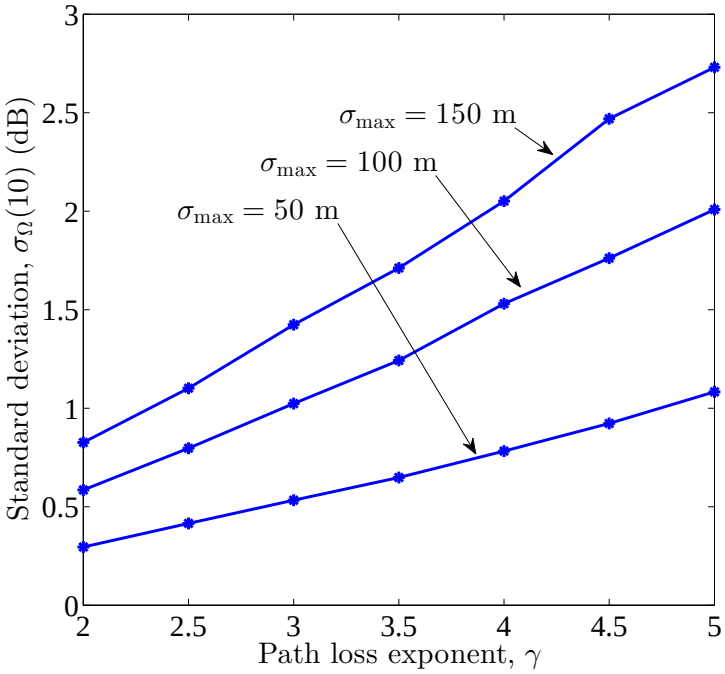

Fig. 5. The standard deviation $\sigma_\Omega(10)$ of the local received power in logarithmic scale for different values of $\sigma_{\max}$ versus the path loss exponent γ.

varying path loss, whereas $\sigma_\Omega(l)$ depicts the time-varying shadow fading. The variations of these two in l confirm that the proposed channel model is non-stationary. From this figure, it can also be concluded that the spread $\sigma_\Omega(l)$ of the local received power is a concave function[7] of l with a maximum at $l = 10$ and two zeros at $l = 0$ and $l = 20$.

Fig. 8 exhibits the local PDP $S_{\tau'}(\tau'; l)$ (see (18)) in the position index l, where $\sigma_{\max} = 50\,\mathrm{m}$. The variations of $S_{\tau'}(\tau'; l)$ in l once again verify that the proposed channel model is non-

[7]Although, the local received power $\Omega(l)$ is a stochastic process with the first-order density $p_{\mathbf{\Omega}}(\omega; l)$ given by (15), its spread $\sigma_\Omega(l)$ is a deterministic function obtained by averaging, i.e., $\sigma_\Omega(l) = [E\{(\Omega(l) - E\{\Omega(l)\})^2\}]^{1/2}$. The mathematical complexity of (15) does not allow us to provide a closed-form solution for the spread $\sigma_\Omega(l)$ (and the mean $m_\Omega(l)$). Therefore, we are not able to show the concavity of the spread $\sigma_\Omega(l)$, analytically. However, the numerical results in Fig. 7 show that this function is concave in l. In addition, since the starting and the terminating points of each trajectory are fixed (independent of the realization), while the maximum variations of the trajectory $\mathcal{T}$ occur almost at the middle of the travelling path [16], it can heuristically be understood that the spread $\sigma_\Omega(l)$ has a concave shape in l.

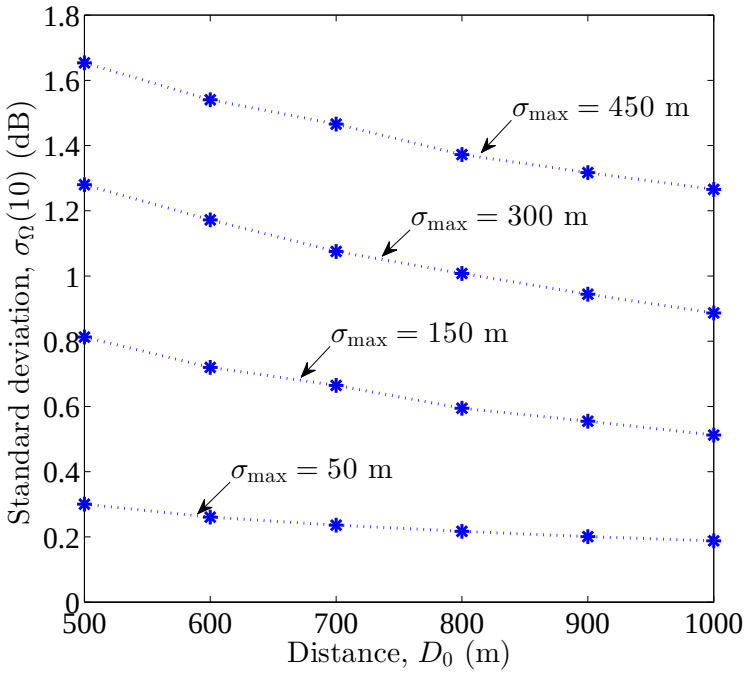

Fig. 6. The standard deviation $\sigma_\Omega(10)$ of the local received power in logarithmic scale for different values of $\sigma_{\max}$ versus the distance D_0 of the BS from the origin.

stationary. In this figure, different colours have been used to distinguish the contribution of each scatterer to the PDP $S_{\tau'}(\tau'; l)$. These colours are the same as those chosen in Fig. 2. As an example, the scatterer S_4 (located at the north east of the MS) is shown in purple (see Fig. 2). At $l = 0$, this scatterer has the greatest distance to the MS (the origin), thus the wave retransmitted from S_4 results in the largest delay $\tau_4'(0)$ component as shown in Fig. 8. Referring to Fig. 2, the total travelling distance of the 4th plane wave ($\tau_4'(l)$), however, decreases when the MS moves toward the destination point, which is located in a close vicinity of S_4. This can also be observed in Fig. 8, where the purple part (associated with $\tau_4'(l)$) of the plot tends to smaller delays as l increases. The contribution of the other scatterers can also be tracked in Fig. 8. This is, however, difficult if the number of scatterers increases. It is also noteworthy that for a given l, the farthest (nearest) scatterer to the MS results in the lowest (highest) PDP $S_{\tau'}(\tau'; l)$ as shown in Fig. 8. This can be confirmed by the fact that the power of each plane wave decreases by increasing

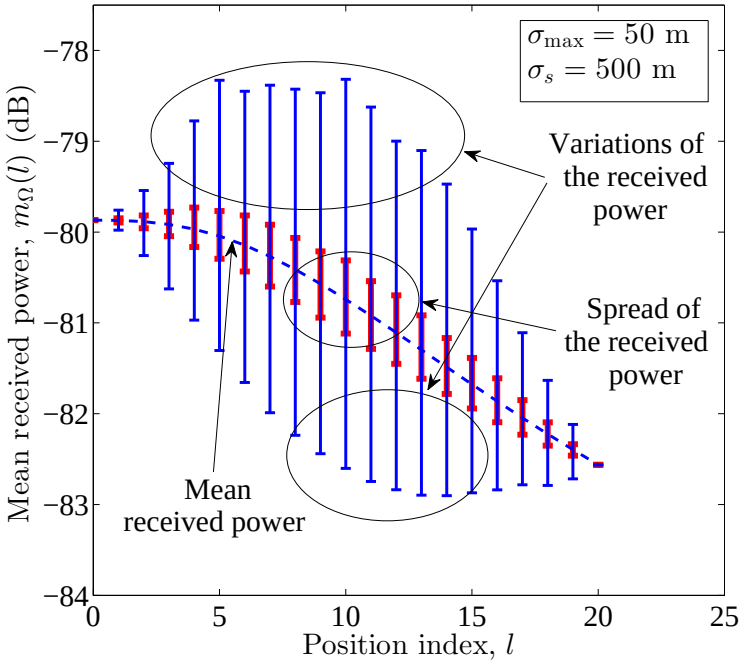

Fig. 7. The mean received power (path loss) $m_\Omega(l)$ as well as the spread $\sigma_\Omega(l)$ of the local received power (shadow fading) in the position index l.

its travelling distance, which has been modelled by $\boldsymbol{c}_n(l) = C\boldsymbol{D}_n^{-\gamma/2}(l)$ in this paper. Another important observation in Fig. 8 is the variation of the delay spread in l. As can be observed, the delay spread first increases and then decreases (look at each colour and follow its spread when l increases). Since the starting and the terminating point of the trajectory are always fixed, the PDFs $p_{\boldsymbol{\tau'}_n}(\tau';0)$ and $p_{\boldsymbol{\tau'}_n}(\tau';L)$ tend to the delta function located at $\boldsymbol{\tau'}_n(0)$ and $\boldsymbol{\tau'}_n(L)$, respectively. For visual reasons, however, we omit these delta functions (associated with each scatterer). The observed maximum delay spread at $l = 10$ can be attributed to the fact that the maximum variations of $\mathcal{T}$ happen almost in the middle of the travelling path (see Section IV).

Fig. 9 represents the local Doppler PSD $S_{\mu\mu}(f;l)$ (see (20)) in the position index l, where $\sigma_{\max}$ has been set to 50 m. The interpretation of this figure is very similar to that of the previous one, but in the frequency domain. Referring to Fig. 2, for all values of l, the wave emitted from S_1 arrives at the MS with the AOA $\boldsymbol{\alpha}_n^R(l)$ almost equal to the AOM $\boldsymbol{\alpha}_v(l)$ of the MS.

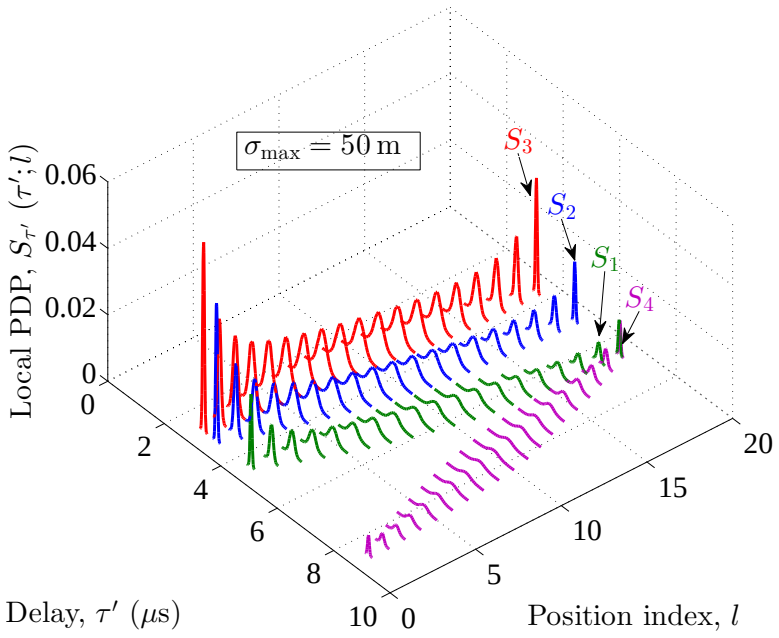

Fig. 8. The local PDP $S_{\tau'}(\tau';l)$ (see (18)) in the position index l, illustrating the contribution of each scatterer.

Therefore, this scatterer causes the maximum negative Doppler shift of about -60 Hz (see the green part of the plot). On the contrary, the scatterer located almost always in the front of the MS, i.e., S_4 results in the maximum positive Doppler shift of about 60 Hz (see the purple part of the plot). Nevertheless, the Doppler PSD $S_{\mu\mu}(f;l)$ associated with S_4 is much smaller than that pertinent to S_1. The reason is that the travelling distance of the 4th plane wave is much longer than that of the first scatterer S_1, thus the attenuation effect is much higher. Also worth mentioning is that the red part (associated with S_3) of the Doppler PSD $S_{\mu\mu}(f;l)$. This part starts with a positive mean Doppler shift and ends with a negative one. This variation can be tracked in Fig. 2, where the wave retransmitted from S_3, first arrives at the front of the MS and then at its back. The hole in the figure is simply due to the absence of some particular Doppler shifts, which cannot be generated according to the propagation model in Fig. 2. However, at the corresponding position indices, other Doppler shifts exist due to the arrivals from all scatterers (look along the frequency axis, e.g., at $l = 10$). The variations of the Doppler spread along l

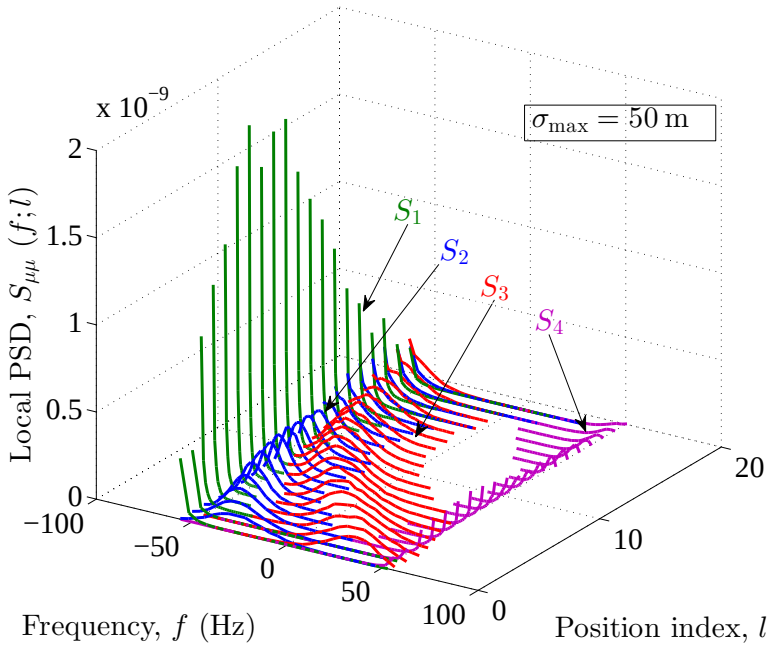

Fig. 9. The local Doppler PSD $S_{\mu\mu}(f;l)$ (see (20)) in the position index l, illustrating the contribution of each scatterer.

can be explained in the same way as for the delay spread. An important difference, however, is that the Doppler PSD $S_{\mu\mu}(f;l)$ does not tend to the delta function at $l = 0$ ($l = 19$), as the AOM $\boldsymbol{\alpha}_v(0)$ ($\boldsymbol{\alpha}_v(19)$) of the MS varies from realization to realization.

VIII. Conclusion

This paper has introduced a new approach for modelling non-stationary mobile fading channels. The new approach is based on random trajectories of the MS, rather than random distributions of scatterers. The new approach enables us to obtain required channel characteristics even if the number of scatterers is very limited. A random trajectory model based on the primitives of BFs has been utilized to develop a non-stationary channel model that captures multi-scale fading. The new model is physically explainable, as it is based on the additive multipath fading propagation mechanism. To model the path loss, the path gains have been determined by the travelling distance of the corresponding plane waves, while the randomness of each distance

generates large-scale fading. In this context, it has been shown that the local received power follows closely a Gaussian process in logarithmic scale, while the envelope of the channel can be well-approximated by a Suzuki process. The Suzuki process is reported to be the best for the modelling of real-life channels showing different scales of fading. It has been demonstrated that the proposed model enables two degrees of freedom to control the spread of shadow fading, while this spread is weakly affected by the position of the BS. The local PDP process and the local Doppler PSD process have also been studied. It has been shown that these quantities vary in position, confirming that the proposed channel is non-stationary. Simulation results have shown that the contribution of each scatterer to these quantities can be tracked individually if the channel is sparse enough.

In future works, the new approach can be applied to develop new channel models with other objectives than capturing multi-scale fading. In addition, the utilized random trajectory model in this paper can be substituted by other random trajectory models to see whether the same performance can be obtained or not.

APPENDIX A
PROOF OF THEOREM 1

It has been shown in [16] that the first-order density of $\boldsymbol{x}(l)$ in (1) is a normal distribution of the form $N(m_{\boldsymbol{x}}(l), \sigma^2_{\boldsymbol{x}}(l))$, where the mean $m_{\boldsymbol{x}}(l)$ and the variance $\sigma^2_{\boldsymbol{x}}(l)$ are given by $x_s + l\delta_x$ and

$$\sigma^2_{\boldsymbol{x}}(l) = \sigma^2_x \frac{l^2 L}{3}\left(1 - \frac{l}{L}\right)^2 \tag{21}$$

respectively. The same statement holds for the first-order density of $\boldsymbol{y}(l)$, provided that the index x is replaced by y. This allows us to conclude that $(x_n^S - \boldsymbol{x}(l))$ and $(y_n^S - \boldsymbol{y}(l))$ are also normal processes of the form $N(x_n^S - m_{\boldsymbol{x}}(l), \sigma^2_{\boldsymbol{x}}(l))$ and $N(y_n^S - m_{\boldsymbol{y}}(l), \sigma^2_{\boldsymbol{y}}(l))$, respectively. The process $\boldsymbol{D}_n^{S-MS}(l)$ can then be considered as the envelope of a complex Gaussian distribution with $(x_n^S - \boldsymbol{x}(l))$ and $(y_n^S - \boldsymbol{y}(l))$ as its inphase and quadrature components. The phase and the envelope of complex Gaussian processes with correlated quadratures and non-identical means (variances) have been studied in [44] and [45]. Herein, the correlation ρ between the inphase and quadrature components is zero, as $\boldsymbol{x}(l)$ and $\boldsymbol{y}(l)$ are independent processes (see [16]). Setting

$\rho = 0$ in the envelope distribution in [45, Eq. (1)], and assuming $\sigma_x = \sigma_y$ gives

$$\begin{aligned} p_{\boldsymbol{D}_n^{S-MS}}(d'_n; l) &= \frac{d'_n}{\sigma^2_{\boldsymbol{x}}(l)} \exp\left\{ -\frac{(x_n^S - m_{\boldsymbol{x}}(l))^2 + (y_n^S - m_{\boldsymbol{y}}(l))^2 + {d'}_n^2}{2\sigma^2_{\boldsymbol{x}}(l)} \right\} \\ &\times I_0\left(\frac{\sqrt{(x_n^S - m_{\boldsymbol{x}}(l))^2 + (y_n^S - m_{\boldsymbol{y}}(l))^2}}{\sigma^2_{\boldsymbol{x}}(l)} d'_n \right). \end{aligned} \tag{22}$$

With reference to (4), the total distance process $\boldsymbol{D}_n(l) = D_n^{BS-S} + \boldsymbol{D}_n^{S-MS}(l)$ is a linear function of $\boldsymbol{D}_n^{S-MS}(l)$. Considering the first-order density $p_{\boldsymbol{D}_n^{S-MS}}(d'_n; l)$ of $\boldsymbol{D}_n^{S-MS}(l)$ in (22) and applying the concept of transformation of random variables gives the PDF in (5).

APPENDIX B
PROOF OF (14)

The local received power averaged over the phase is obtained as follows

$$\begin{aligned} \boldsymbol{\Omega}(l) &= E\left\{ |\boldsymbol{\mu}(t_l)|^2 \right\} \\ &= E\left\{ \boldsymbol{\mu}^*(t_l) \boldsymbol{\mu}(t_l) \right\} \\ &= \sum_{n=1}^{N} \sum_{m=1}^{M} \boldsymbol{c}_n(t_l) \boldsymbol{c}_m(t_l) e^{j\left[2\pi \int_{-\infty}^{t_l} (\boldsymbol{f}_m(t'_l) - \boldsymbol{f}_n(t'_l)) dt'_l - k_0(\boldsymbol{D}_m(t_l) - \boldsymbol{D}_n(t_l))\right]} E\left\{ e^{j(\boldsymbol{\phi}_m - \boldsymbol{\phi}_n)} \right\} \\ &= \sum_{n=1}^{N} \boldsymbol{c}_n^2(t_l) \end{aligned} \tag{23}$$

in which $E\left\{ e^{j(\boldsymbol{\phi}_m - \boldsymbol{\phi}_n)} \right\} = 1$ has been used for $m = n$ and $E\left\{ e^{j(\boldsymbol{\phi}_m - \boldsymbol{\phi}_n)} \right\} = 0$ for any $m \neq n$ (see SectionV). The result in (23) indicates that the mean power is equal to the sum of powers carried out by the individual multipath waves, which is known as the conservation-of-power law [50].

REFERENCES

[1] A. Ispas, G. Ascheid, C. Schneider, and R. Thomä, "Analysis of local quasi-stationarity regions in an urban macrocell scenario," in *Proc. 71th IEEE Vehicular Technology Conference, VTC 2010-Spring*. May 2010, Taipei, Taiwan.

[2] A. Gehring, M. Steinbauer, I. Gaspard, and M. Grigat, "Empirical channel stationarity in urban environments," in *Proc. 4th European Personal Mobile Communications Conference*. Feb. 2001, Vienna, Austria.

[3] D. Umansky and M. Pätzold, "Stationarity test for wireless communication channels," in *Proc. IEEE Global Communications Conference, IEEE GLOBECOM 2009*. Nov./Dec. 2009, Honolulu, Hawaii, USA.

[4] A. Paier, J. Karedal, N. Czink, H. Hofstetter, C. Dumard, T. Zemen, F. Tufvesson, A. F. Molisch, and C. F. Mecklenbräucker, "Characterization of vehicle-to-vehicle radio channels from measurement at 5.2 GHz," *Wireless Personal Communications (WPC)*, vol. 50, no. 1, pp. 19–32, July 2009.

[5] A. Ghazal, C. X. Wang, B. Ai, D. Yuan, and H. Haas, "A non-stationary wideband MIMO channel model for high-mobility intelligent transportation systems," *IEEE Trans. on Intelligent Transportation System, In press*, vol. 16, no. 2, pp. 885–897, Apr. 2015.

[6] F. M. Schubert, M. L. Jakobsen, and B. H. Fleury, "Non-stationary propagation model for scattering volumes with an application to the rural LMS channel," *IEEE Trans. Antennas Propag.*, vol. 61, no. 5, pp. 2817–2828, May 2013.

[7] A. Chelli and M. Pätzold, "A non-stationary MIMO vehicle-to-vehicle channel model based on the geometrical T-junction model," in *Proc. International Conference on Wireless Communications and Signal Processing, WCSP 2009*. Nov. 2009, Nanjing, China.

[8] A. Borhani and M. Pätzold, "A novel non-stationary channel model utilizing Brownian random paths," *REV Journal on Electronics and Communications*, vol. 4, no. 1-2, pp. 8–15, Jan. 2014.

[9] J. Karedal, F. Tufvesson, N. Czink, A. Paier, C. Dumard, T. Zemen, C. F. Mecklenbräuker, and A. F. Molisch, "A geometry-based stochastic MIMO model for vehicle-to-vehicle communications," *IEEE Trans. Wireless Commun.*, vol. 8, no. 7, pp. 3646–3657, July 2009.

[10] A. Chelli and M. Pätzold, "A non-stationary MIMO vehicle-to-vehicle channel model derived from the geometrical street model," in *Vehicular Technology Conference, VTC-Fall 2011 IEEE*, Sept 2011, pp. 1–6.

[11] L. Bernadó, T. Zemen, F. Tufvesson, A.F. Molisch, and C. F. Mecklenbräuker, "Delay and doppler spreads of nonstationary vehicular channels for safety-relevant scenarios," *Vehicular Technology, IEEE Transactions on*, vol. 63, no. 1, pp. 82–93, Jan 2014.

[12] G. Matz, "On non-WSSUS wireless fading channels," *IEEE Trans. Wireless Commun.*, vol. 4, no. 5, pp. 2465–2478, Sept. 2005.

[13] P. Kyösti et al., "WINNER II channel models, DR1.1.2," *available in: https://www.ist-winner.org/WINNER2- Deliverables/D1.1.2.zip*, 2007.

[14] L. Liu, C. Oestges, J. Poutanen, K. Haneda, P. Vainikainen, F. Quitin, F. Tufvesson, and P. D. Doncker, "The COST 2100 MIMO channel model," *Wireless Communications, IEEE*, vol. 19, no. 6, pp. 92–99, December 2012.

[15] A. Borhani and M. Pätzold, "A non-stationary one-ring scattering model," in *Proc. IEEE Wireless Commun. and Net. Conf. (WCNC'13)*. Apr. 2013, Shanghai, China.

[16] A. Borhani and M. Pätzold, "A highly flexible trajectory model based on the primitives of Brownian fields—part I: Fundamental principles and implementation aspects," *IEEE Trans. Wireless Commun.*, vol. 14, no. 2, pp. 770–780, Feb. 2015.

[17] A. Borhani and M. Pätzold, "A highly flexible trajectory model based on the primitives of Brownian fields—part II: Analysis of the statistical properties," *IEEE Trans. Wireless Commun., DOI: 10.1109/TWC.2015.2470257*, Aug. 2015.

[18] J. Salo, L. Vuokko, H. M. El-Sallabi, and P. Vainikainen, "An additive model as a physical basis for shadow fading," *IEEE Trans. Veh. Technol.*, vol. 56, no. 1, pp. 13–26, Jan 2007.

[19] H. Suzuki, "A statistical model for urban radio propagation," *IEEE Trans. Commun.*, vol. 25, no. 7, pp. 673–680, July 1977.

[20] F. Hansen and F. I. Meno, "Mobile fading—Rayleigh and lognormal superimposed," *IEEE Trans. Veh. Technol.*, vol. 26, no. 4, pp. 332–335, Nov. 1977.

[21] M. J. Marsan, G. C. Hess, and S. S. Gilbert, "Shadowing variability in an urban land mobile environment at 900 MHz," *Electronics Letters*, vol. 26, no. 10, pp. 646–648, May 1990.

[22] J. E. Berg, R. Bownds, and F. Lotse, "Path loss and fading models for microcells at 900 MHz," in *Vehicular Technology Conference, IEEE 42nd*, May 1992, pp. 666–671.

[23] S. Mockford, A. M. D. Turkmani, and J. D. Parsons, "Local mean signal variability in rural areas at 900 MHz," in *Vehicular Technology Conference, 1990 IEEE 40th*, May 1990, pp. 610–615.

[24] A. Mawira, "Models for the spatial correlation functions of the (log)-normal component of the variability of VHF/UHF field strength in urban environment," in *Third IEEE Int. Symp. on Personal, Indoor and Mobile Radio Communications, PIMRC '92.*, Oct. 1992, pp. 436–440.

[25] S. Kozono and K. Watanabe, "Influence of environmental buildings on UHF land mobile radio propagation," *IEEE Trans. Commun.*, vol. 25, no. 10, pp. 1133–1143, Oct. 1977.

[26] N. B. Mehta, J. Wu, A. F. Molisch, and J. Zhang, "Approximating a sum of random variables with a lognormal," *IEEE Trans. Wireless Commun.*, vol. 6, no. 7, pp. 2690–2699, July 2007.

[27] A. F. Molisch, "Ultrawideband propagation channels-theory, measurement, and modeling," *IEEE Trans. Veh. Technol.*, vol. 54, no. 5, Sept. 2005.

[28] K. T. Wong, Y. I. Wu, and M. Abdulla, "Landmobile radiowave multipaths' DOA-distribution: Assessing geometric models by the open literature's empirical datasets," *IEEE Trans. Antennas Propag.*, vol. 58, no. 2, pp. 946–958, Feb. 2010.

[29] A. Borhani and M. Pätzold, "A unified disk scattering model and its angle-of-departure and time-of-arrival statistics," *IEEE Trans. Veh. Technol.*, vol. 62, no. 2, pp. 473–485, Feb. 2013.

[30] T. Camp, J. Boleng, and V. Davies, "A survey of mobility models for ad hoc network research," *Wireless Communications and Mobile Computing*, vol. 2, no. 5, pp. 483–502, Sept. 2002.

[31] F. Bai and A. Helmy, "A survey of mobility modeling and analysis in wireless adhoc networks," in *Wireless Ad Hoc and Sensor Networks*. Springer, Oct. 2006, ISBN 978-0-387-25483-8.

[32] J. Härri, F. Filali, and C. Bonnet, "Mobility models for vehicular ad hoc networks: a survey and taxonomy," *IEEE Communications Surveys & Tutorials*, vol. 11, no. 4, pp. 19–41, 2009.

[33] K. B. Baltzis, "A simplified geometric channel model for mobile-to-mobile communications," *Radioengineering*, vol. 20, no. 4, pp. 961–967, Dec. 2011.

[34] R. Almesaeed, A. S. Ameen, A. Doufexi, N. Dahnoun, and A. R. Nix, "A comparison study of 2D and 3D ITU channel model," in *Wireless Days (WD), 2013 IFIP, Valencia*, Nov 2013, pp. 1–7.

[35] M. Pätzold and A. Borhani, "A non-stationary multipath fading channel model incorporating the effect of velocity variations of the mobile station," in *Wireless Communications and Networking Conference (WCNC), 2014 IEEE*, April 2014, pp. 182–187.

[36] G. Stüber, *Principles of Mobile Communications*, Springer, 3rd edition, 2011.

[37] B. Boashash, *Time-Frequency Signal Analysis and Processing*, Elsevier Science, 1st edition, 2003.

[38] W. C. Jakes, Ed., *Microwave Mobile Communications*, Piscataway, NJ: IEEE Press, 1994.

[39] M. Pätzold, *Mobile Fading Channels*, Chichester: John Wiley & Sons, 2nd edition, 2011.

[40] T. K. Sarkar, Z. Ji, K. Kim, A. Medouri, and M. Salazar-Palma, "A survey of various propagation models for mobile communication," *Antennas and Propagation Magazine, IEEE*, vol. 45, no. 3, pp. 51–82, June 2003.

[41] C. Phillips, D. Sicker, and D. Grunwald, "A survey of wireless path loss prediction and coverage mapping methods," *Communications Surveys Tutorials, IEEE*, vol. 15, no. 1, pp. 255–270, 2013.

[42] A. Papoulis, *Probability, Random Variables, and Stochastic Processes*, New York: McGraw-Hill, 3rd edition, 1991.

[43] I. S. Gradshteyn and I. M. Ryzhik, *Table of Integrals, Series, and Products*, Elsevier Academic Press, 7th edition, 2007.

[44] V. A. Aalo, G. P. Efthymoglou, and C. Chayawan, "On the envelope and phase distributions for correlated Gaussian quadratures," *IEEE Communications Letters*, vol. 11, no. 12, pp. 985–987, 2007.

[45] P. Dharmawansa, N. Rajatheva, and C. Tellambura, "Envelope and phase distribution of two correlated Gaussian variables," *IEEE Transactions on Communications*, vol. 57, no. 4, pp. 915–921, 2009.

[46] M. Pätzold and G. Rafiq, "Sparse multipath channels: Modelling, analysis, and simulation," in *Personal Indoor and Mobile Radio Communications (PIMRC), 2013 IEEE 24th International Symposium on*, Sept 2013, pp. 30–35.

[47] G. C. Hess, *Handbook of Land-Mobile Radio System Coverage*, Norwood, MA: Artech House, 1997.

[48] A. W. F. Edwards, *Likelihood*, Cambridge University Press, 1992.

[49] B. Kannan et al., "UWB channel characterization in outdoor environments," *IEEE, Tech. Rep. Document IEEE P802.15-15-04-0440-00-004a*, pp. 1–6, Aug. 2004.

[50] G. D. Durgin, *Theory of Stochastic Local Area Channel Modeling for Wireless Communications*, Virginia Polytechnic Institute and State University, PhD Thesis, 2000.